InGaAsP–InP Avalanche Photodiodes for Single Photon Detection

Xudong Jiang, Mark A. Itzler, *Senior Member, IEEE*, Rafael Ben-Michael, and Krystyna Slomkowski

Abstract—In this paper, we describe the design, characterization, and modeling of InGaAsP/InP avalanche diodes designed for single photon detection at wavelengths of 1.55 and 1.06 μm. Through experimental and theoretical work, we investigate critical performance parameters of these single photon avalanche diodes (SPADs), including dark count rate (DCR), photon detection efficiency (PDE), and afterpulsing. The models developed for the simulation of device performance provide good agreement with experimental results for all parameters studied. For 1.55-μm SPADs, we report the relationship between DCR and PDE for gated mode operation under a variety of operating conditions. We also describe in detail the dependence of afterpulsing effects on numerous operating conditions, and in particular, we demonstrate and explain a universal functional form that describes the dependence of DCR on hold-off time at any temperature. For 1.06-μm SPADs, we present the experimentally determined relationship between DCR and detection efficiency for free-running operation, as well as simulations complementing the experimental data.

Index Terms—Avalanche photodiodes, photodiodes, single photon avalanche diodes (SPADs), single photon detection.

I. INTRODUCTION

SINGLE photon detectors are key components for a wide range of applications in the near-infrared (NIR) wavelength range between 1.0 and 1.7 μm, including optical time domain reflectometry [1], quantum cryptography [2], photon-correlation spectroscopy [3], fundamental studies in quantum physics [4], semiconductor device and material characterization [5], laser ranging, and astronomical measurements. These numerous uses for NIR single photon detectors have instigated intensive ongoing research aimed at both fundamental study and practical improvement of the performance of these detectors.

Photomultiplier tubes are widely used as single photon detectors, but their performance at NIR wavelengths is often inadequate, and they suffer from other undesirable attributes including high voltage operation, large size, fragility, and sensitivity to magnetic fields. One of the earliest semiconductor detectors employed for NIR single photon detection was the germanium APD. To reduce false counts in the absence of an optical signal (i.e., dark counts) to an acceptable level, Ge APDs must be cooled to liquid nitrogen temperatures. Apart from the inconvenience of using liquid cryogens, operation at this temperature also makes Ge unsuitable for detecting 1.55-μm photons, since

its cutoff wavelength is ~1.45 μm at 77 K [6]. Silicon APDs are well established, and offer excellent performance for single photon detection at wavelengths in the visible spectra range. However, they suffer from a dramatic reduction in single photon detection efficiency (PDE) for wavelengths beyond 1 μm, and for applications at 1.06 μm, detection efficiencies do not exceed a few percent. Meanwhile, the emergence of new applications requiring NIR single photon detection has spurred an urgent need for improved detector technology. The advent of quantum key distribution (QKD) in fiber-optic networks holds enormous promise for a next generation of encrypted communications [2], [7], and single photon detectors at 1.3 and 1.55 μm are often the most critical components for the overall performance of these systems. Similarly, single photon detection at 1.06 μm in applications, such as lidar, ranging, and imaging will offer next generation performance for systems in which mature laser sources already exist. To achieve high performance single photon detection in the NIR wavelength range, single photon avalanche diodes (SPADs) based on the InGaAsP quaternary material system lattice-matched to InP are likely to provide the most appropriate solution in numerous situations in which sufficiently high performance must be accompanied by high reliability, compact form factor, ease of use, and acceptable cost.

The first work employing InGaAs/InP avalanche photodiodes as single photon detectors at telecom wavelengths was performed by Levine and Bethea in 1984 [8]. In recent years, there has been increasing interest in InGaAs/InP single photon detectors to support the rapid development of QKD and other applications employing telecom wavelength sources, and a great deal of experimental and theoretical work has been reported in this area [9]–[22]. Virtually all of the initial experimental work was focused on characterizing commercially available InGaAs/InP APDs [9]–[15], which were not specifically designed for single photon detection, because dedicated design and fabrication of NIR SPADs was nonexistent until just the last few years. Work on 1.06-μm SPADs has also been performed [23]–[27] within the last five years, with particularly notable accomplishments from researchers at MIT Lincoln Laboratory.

In contrast to the more common "linear mode" operation of APDs below breakdown for which output photocurrent scales linearly with input optical power, SPADs operate in the so-called "Geiger mode." Geiger mode operation is achieved by applying a reverse bias exceeding the breakdown voltage so that the photoexcitation of just a single charge carrier can lead to a self-sustaining avalanche, producing a macroscopic current pulse that can be sensed using an appropriate threshold detection circuit. Key parameters limiting the performance of SPAD-based systems include the photon detection efficiency (PDE), the dark

count rate (DCR) and the afterpulsing probability (AP). These parameters are affected by many factors, including the material quality, device design, and operating conditions.

In this paper, we describe the design, characterization, and modeling of InGaAsP/InP SPADs for single photon detection at 1.55 and 1.06 μm. In Section II, general considerations for the design of SPADs and the resulting device structure are described. In Section III, we outline a versatile formalism for modeling SPAD performance. In Sections IV and V, we present experimental results for 1.55- and 1.06-μm SPADs, respectively, along with detailed comparisons to simulation results. Conclusions are summarized in Section VI.

II. GENERAL CONSIDERATIONS FOR SPAD DESIGN

The DCR of a SPAD is the probability of detecting an avalanche in the absence of an incident photon, and it arises from "dark" carriers generated in the SPAD structure when no input photons are present. The mechanisms involved in dark carrier generation include thermal and field-mediated (i.e., tunneling) effects. Although the average DCR can be subtracted from measurements intended to extract signal count rates, the time-dependent fluctuations in DCR constitute a noise contribution in SPAD performance, and are analogous to shot noise in context of analog (e.g., linear mode) APDs. Complementing DCR is the PDE, which is the probability that an input photon is in fact detected by the SPAD. The PDE is the product of the probability that an input photon is absorbed (i.e., the absorption region quantum efficiency) and the probability that a resulting photo-excited carrier leads to a runaway avalanche (i.e., the avalanche probability P_a).

A primary goal of SPAD device design is to optimize the device structure and resulting electric field profile to minimize DCR while maximizing PDE. From the point of view of material quality, the defect concentration in the SPAD structure should be minimized to reduce defect-mediated performance degradation. Examples of undesirable defect-related phenomena include trap-assisted tunneling (TAT), thermal generation of carriers via midgap or deep levels, and afterpulsing effects (explained later) arising from trapping and detrapping of carriers at defects in the multiplication region. In particular, the identification of the specific defect types involved in these various processes, as well as an understanding of their origin in the material fabrication process is of great importance for further device performance improvement. With regard to device operating conditions, for applications in which single photon arrival times are accurately known (such as QKD), system performance in the presence of significant DCR can be improved dramatically using gated mode operation. In gated mode, the SPAD is "armed" by biasing above the breakdown voltage for a relatively short period of time coincident with the known photon arrival time. Since the probability of registering a dark count is proportional to the gate duration, shorter gate periods can be used to effectively reduce the dark count probability per gate.

Once an avalanche is generated, it needs to be detected and quenched. The detection process generally entails comparison of the detector signal with a preset threshold, and provides a purely
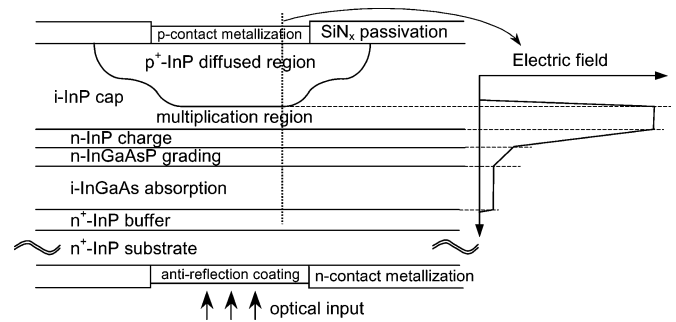

Fig. 1.   Schematic representation of APD design platform.

digital output. Quenching of the avalanche can be achieved in several ways. Gated quenching is accomplished using gated mode operation in which the SPAD remains armed until the bias voltage is brought below the breakdown voltage V_{br} according to the fixed gate pulse duration. In contrast to gated operation, free-running operation leaves the SPAD in its armed state continuously until an avalanche event is detected. When free-running, a SPAD can be quenched either passively or actively. Passive quenching uses a resistor in series with the SPAD to drop the SPAD bias voltage below V_{br} when a sufficiently large avalanche current is induced. Although the passive quench process is fast, resetting the device to the armed state is generally slow, as dictated by the RC time constant of the quench resistor R and device capacitance C. Active quenching employs circuitry to sense the avalanche onset, actively force the SPAD bias below V_{br} to quench the avalanche, and then rapidly reset the SPAD to its armed state.

Afterpulsing is caused by the trapping and subsequent release (detrapping) of carriers induced during previous avalanches. As with "primary" dark carriers, a detrapped carrier can trigger avalanches, and leads to increased DCRs. The detrapping process can be characterized by a detrapping lifetime, which decreases with increasing temperature. Afterpulsing effects can be made arbitrarily small by implementing a sufficiently long hold-off time between gate pulses, but this approach can be quite restrictive with respect to repetition rate in the gated mode operation and count rate in free-running operation. Afterpulsing also forces tradeoffs with respect to operating temperature: lower temperature operation reduces DCR but generally exacerbates afterpulsing effects. The reduction of afterpulsing effects can be achieved if the defects responsible for carrier trapping can be identified and eliminated. Moreover, a better understanding of the dependence of the detrapping process on local electric fields would aid design optimization for the SPAD electric field profile. With respect to operating conditions, since the number of trapped carriers per avalanche scales with the number of carriers created during the avalanche, afterpulsing can be reduced by minimizing the number of primary carriers flowing through the multiplication region by using shorter gate durations and lower bias voltages.

With consideration for the design goals and concepts outlined earlier, we have developed a SPAD device design platform, illustrated in Fig. 1, employing a separate absorption and
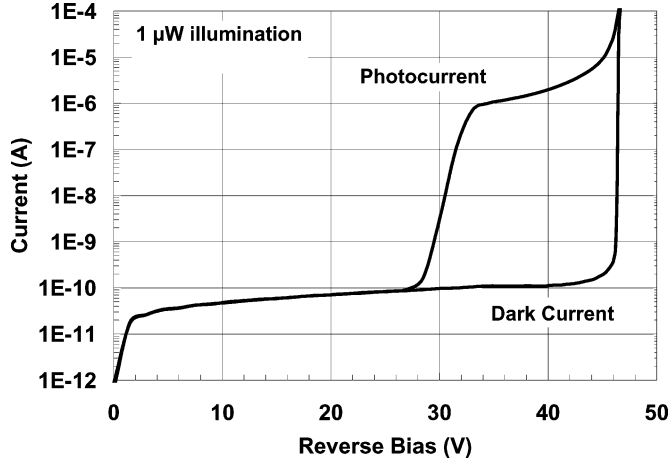
Fig. 2. Typical dark and illuminated (1-μW) I-V characteristics for a 25-μm diameter SPAD at 293 K.

multiplication (SAM) structure [28]. An n$^+$-InP buffer layer is grown on an n$^+$-InP substrate, followed by an absorption layer with appropriate cutoff wavelength (Fig. 1 shows an In$_{0.53}$Ga$_{0.47}$As absorber with a 295-K cutoff wavelength of $\sim$1.67 μm). The valence band offset at an abrupt InGaAs(P)/InP heterojunction causes hole trapping [29], and three to six In-GaAsP grading layers are inserted between the In$_{0.53}$Ga$_{0.47}$As and InP layers of the structure to reduce the effective trap depth for holes. Adjacent to the grading layer is a charged layer that allows for more flexible tailoring of the internal electric field profile in the device structure. The final epitaxial layer is an un-doped InP cap layer. During device fabrication, the active region is determined by the patterning of a SiN dielectric passivation layer to create a diffusion mask, and a subsequent diffusion of Zinc dopant atoms creates a p$^+$-InP region within the undoped InP cap layer. The thickness of the multiplication region is con-trolled by the Zn diffusion depth. The quasi-cylindrical junction formed by a single diffusion exhibits electric field enhancement where the junction curvature is maximum, and leads to prema-ture avalanche breakdown at the edge of the device. A double diffusion process [30] is, therefore, used to tailor the junction profile and create a deeper junction in the central part of the ac-tive region. The resulting gain profile across the center part of the active region is uniform with the gain being reduced in the pe-ripheral region of the device. This planar buried-junction design utilizing high-quality SiN passivation can guarantee extremely stable long-life performance (e.g., >25 years of operation for telecom receivers) [31]–[33].

Fig. 2 shows linear mode I-V characteristics for a typical 25-μm active area diameter SPAD. The active area diameter is determined by the more deeply diffused region (see Fig. 1), and defines the optically active region of the device. We oper-ationally define the breakdown voltage V_{br} as the voltage for which the linear mode dark current I_d reaches 10 μA. The onset of the photocurrent response at the punchthrough voltage V_p oc-curs when the depletion region first extends into the absorption layer. The smooth increase in photocurrent to gains in excess of 100 (before V_{br} is reached) is consistent with a uniform gain profile and the absence of edge breakdown.

III. SPAD DEVICE PERFORMANCE MODELING

There are a number of mechanisms that generate carriers in a SPAD structure, including thermally-generated or tunneling-generated bulk dark carriers and background- or signal-photon-generated photocarriers. In Geiger mode operation, these carri-ers have a finite probability P_a of initiating an avalanche if they reach the multiplication region.

The thermal generation rate per unit volume N_{th} is deter-mined principally by Shockley–Read–Hall (SRH) processes, and can be expressed as

$$N_{\text{th}} = \frac{n_i}{\tau_{\text{SRH}}} \tag{1}$$

where n_i is the intrinsic carrier concentration and τ_{SRH} is the lifetime related to SRH processes.

Tunneling processes include direct band-to-band tunneling (BBT) and TAT. The dark carrier generation rate per unit volume due to BBT can be expressed as [34]

$$N_{\text{BBT}} = \sqrt{\frac{2m_r}{E_g}} \frac{q^2 F^2}{4\pi^3 \hbar^2} \exp\left(-\frac{\pi\sqrt{m_r E_g^3}}{2\sqrt{2}q\hbar F}\right) \tag{2}$$

where m_r is the reduced mass of the conduction band effective mass m_c and the light hole effective mass m_{lh}, i.e., $1/m_r = 1/m_c + 1/m_{\text{lh}}$. E_g is the bandgap, q is the electron charge, and $\hbar$ is the reduced Planck's constant. F is the position-dependent electric field.

TAT is a complex process, with dependences on the position of trap inside the energy gap, the density of traps, trap occupation by electrons, and the trap potential. In recent modeling work, Donnelly et al. [24] set the tunneling current from the valence band to the trap equal to the tunneling current from the trap to the conduction band to determine the filling of the traps and obtain an explicit formula for the TAT current. By adopting this procedure, the dark carrier generation rate per unit volume due to TAT can be expressed as

$$N_{\text{TAT}} = \frac{\sqrt{\frac{2m_r}{E_g}} \frac{q^2 F^2}{4\pi^3 \hbar^2} N_{\text{Trap}} \exp\left(-\frac{\pi\sqrt{m_{\text{lh}} E_{B1}^3} + \pi\sqrt{m_c E_{B2}^3}}{2\sqrt{2}q\hbar F}\right)}{N_v \exp\left(-\frac{\pi\sqrt{m_{\text{lh}} E_{B1}^3}}{2\sqrt{2}q\hbar F}\right) + N_c \exp\left(-\frac{\pi\sqrt{m_c E_{B2}^3}}{2\sqrt{2}q\hbar F}\right)} \tag{3}$$

where the barrier heights E_{B1} and E_{B2} govern tunneling from valence band to trap and trap to conduction band, respectively. N_v and N_c are the effective density of states for the valence and conduction bands, respectively. N_{trap} is the trap concentration.

For calculating the breakdown voltage, a suitable model for ionization coefficients is required. Dead space effects have been found to play an important role in APDs with thin multipli-cation widths [35], [36]. However, for appropriately designed SPADs, multiplication widths are generally relatively thick, and it is reasonable to use a canonical local field model in which ionization coefficients depend only on field. We adopted the physical model of Zappa et al. [37], which takes into account the dependence of ionization coefficients on temperature. To calculate the count rate and detection efficiency, it is important to know the avalanche probability, and we adopted the model of

McIntyre [38] for this purpose. The model of Adachi [39] was used for the calculation of absorption coefficient, and the effects of electroabsorption [40] and free carrier absorption have also been included.

For the parameters used in the calculation, the effective mass of electrons and holes and the change of bandgap energy with temperature were taken from [41]. Three important parameters—SRH lifetime τ_{SRH}, trap density N_{trap}, and trap energy level E_{trap}—remain to be determined. From fitting of our simulated results to the measured results, we find $\tau_{\mathrm{SRH}} \sim 70\,\mu\mathrm{s}$. There have been past studies of the traps in InP [42]–[47] and $\mathrm{In}_{0.53}\mathrm{Ga}_{0.47}\mathrm{As}$ [42], [43], [48]–[51], but there is no general agreement on the type, capture cross section, energy level, and concentration of traps in state-of-the-art epitaxially grown samples of these materials. Following Donnelly *et al.* [24], we define a parameter $\alpha = (E_{\mathrm{trap}} - E_{v0})/E_g$ to identify the position of traps inside the energy bandgap, where E_{trap} is the energy level of trap and E_{v0} is the top of valence band. For the trap level in $\mathrm{In}_{0.53}\mathrm{Ga}_{0.47}\mathrm{As}$, we adopted the value of [42], i.e., $\alpha(\mathrm{In}_{0.53}\mathrm{Ga}_{0.47}\mathrm{As}) \sim 0.78$. For the trap level in InP, we adopted the value of [47], i.e., $\alpha(\mathrm{InP}) \sim 0.75$. Based on fitting results, for the trap concentrations we use $N_{\mathrm{trap}}\,(\mathrm{In}_{0.53}\mathrm{Ga}_{0.47}\mathrm{As}) \sim 1 \times 10^{15}\,\mathrm{cm}^{-3}$, $N_{\mathrm{trap}}\,(\mathrm{InP}) \sim 2 \times 10^{14}\,\mathrm{cm}^{-3}$ for both the 1.55- and 1.06-μm devices. For trap energy level and concentrations in layers other than InP and $\mathrm{In}_{0.53}\mathrm{Ga}_{0.47}\mathrm{As}$, we use a linear interpolation based on the energy bandgap of each layer.

According to [19], assuming Poissonian statistics for the detection of dark counts, the dark count probability P_d can be expressed as

$$P_d = 1 - \exp\left(-P_a\, N_d\right) \qquad (4)$$

where P_a is the avalanche probability and N_d is the number of dark carriers. N_d contains the contributions expressed as

$$
\begin{aligned}
N_d = {} & N_{\mathrm{DM1}}\,\tau + N_{\mathrm{DM2}}\,\tau_{\mathrm{tr}}\,\boldsymbol{M}_0 \\
& + P_d\,\frac{c}{1-c}\,M_g\,\frac{\exp\left(\tau/\tau_d\right)-1}{\exp\left(\Delta T/\tau_d\right)-1} \\
& + P_d\,\frac{c}{1-c}\,M_g\,\frac{\exp\left(\tau_{\mathrm{tr}}/\tau_d\right)-1}{\exp\left(\Delta T/\tau_d\right)-1} \qquad (5)
\end{aligned}
$$

where the first two terms correspond to the primary dark carriers at $V_{\mathrm{op}} = V_{\mathrm{br}} + \Delta V_{\mathrm{ex}}$ and V_{dc}, respectively. V_{br} is the breakdown voltage, ΔV_{ex} is the excess bias beyond V_{br}, and V_{dc} is the voltage maintained during hold-off periods when the SPAD is not armed. N_{DM1} and N_{DM2} are the dark carrier generation rates at V_{op} and V_{dc}, and can be calculated using (1)–(3). τ is the gate pulse width, ΔT is the gate pulse period, and τ_{tr} is the effective transit time of carriers created at V_{dc}. M_0 is the dc gain at V_{dc}. The last two terms in (5) are the dark carriers caused by afterpulsing: the third term is the number of carriers detrapped during the gate pulse, and the fourth term is the number of carriers detrapped preceding the gate pulse by a time interval less than τ_{tr}. Here, c is the ratio of the number of trapped carriers to the total number of carriers generated per avalanche pulse, M_g is the number of carriers created per avalanche, and τ_d is the detrapping time.

When a photon pulse is present, the count probability P_p is given by

$$P_p = 1 - \exp\left(-P_a\, N_p\right) \qquad (6)$$

where the total number of carriers N_p is given by

$$
\begin{aligned}
N_p = {} & N_{\mathrm{DM1}}\tau + N_{\mathrm{DM2}}\tau_{\mathrm{tr}}M_0 + P_p\,\frac{c}{1-c} \\
& \times M_g\left(\frac{\exp\left(\tau/\tau_d\right)-1}{\exp\left(\Delta T/\tau_d\right)-1} + \frac{\exp\left(\tau_{\mathrm{tr}}/\tau_d\right)-1}{\exp\left(\Delta T/\tau_d\right)-1}\right) + \eta\,N_0
\end{aligned}
$$
$$(7)$$

where η is the quantum efficiency and N_0 is the number of photons per pulse.

Following [19], the single photon quantum efficiency (SPQE) is defined as

$$\mathrm{SPQE} = \frac{P_p - P_d}{1 - \exp\left(-N_0\right)}. \qquad (8)$$

Note that the SPQE is closely related to PDE: for sufficiently small dark count probability P_d and photon number N_0, SPQE reduces to $\eta\,P_a$.

Using (1)–(8), we simulate the performance of devices for which the experimental results are presented next, and extracted parameters for (5) and (7) will be presented together with the calculated results.

IV. DEVICE PERFORMANCE OF 1.55-μm SPADs

Due to wafer-level variation of key device fabrication parameters, such as diffusion depth and field control layer doping concentration, devices exhibit wafer-level position-dependent V_{br} and V_p. We have characterized devices from both the center region (hereafter called Ci, where i is the device index) and the edge region (Ei) of the given wafer. Considered as two distinct groups, C and E devices show not only differences in V_{br} and V_p, but also different trap characteristics responsible for afterpulsing effects. In this section, we present the characteristics of these devices related to DCR, SPQE, and afterpulsing.

A. DCR and Dark-Count-Induced Afterpulsing

Experimental data (indicated by symbols) in Fig. 3(a) show [16] the DCR versus hold-off time under four different temperatures for device E1, which has an optical diameter of 40 μm. At each temperature, the device is biased at 0.5 V below V_{br} during the period between gates and 5.5 V above V_{br} when the gate is applied. The gate width was 20 ns, and the hold-off time varied from 4 to 1000 μs. As evident in Fig. 3(a), hold-off times shorter than a temperature-dependent characteristic time lead to a significant increase in the DCR. At lower temperatures, this onset of increased DCR occurs for longer characteristic hold-off times. These phenomena are the result of afterpulsing, and in this section, we present a comprehensive quantitative description of these effects.

In [16], we demonstrated that by properly normalizing and rescaling the DCR versus hold-off time curves at different temperatures, all curves collapse onto a single universal curve. First, for each temperature, DCR values are normalized to the value of
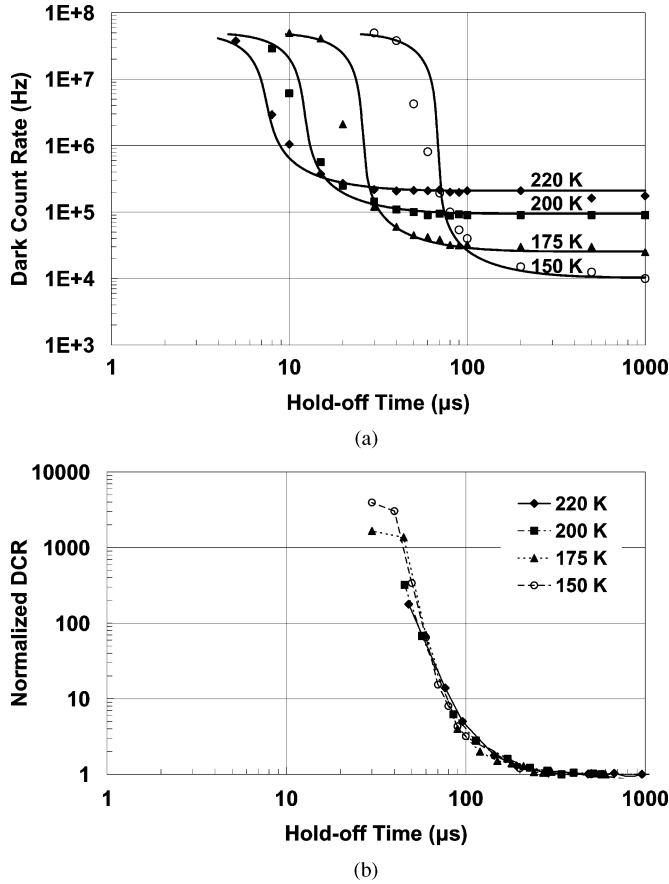
(a)

(b)

Fig. 3. (a) Experimental (symbols) and simulated (solid lines) DCR versus hold-off time for device E1 at four different temperatures. (b) Collapse of data from (a) after normalization and rescaling.

the time-independent background DCR found for long hold-off times. Then, appropriately chosen rescaling factors for the hold-off time axes provide a collapse of all curves to a single curve. Such a collapse is accomplished for the data in Fig. 3(a) using hold-off time axis scaling factors of 1, 3, 5.7, and 9.6 for the 150, 175, 200, and 220 K data, respectively. The resulting collapse is shown in Fig. 3(b). From the dependence of these scaling factors on temperature, an "afterpulsing activation energy" E_{ap} of 91 meV was found. This collapsing behavior basically indicates that the DCR versus hold-off time curves have similar functional forms at different temperatures.

The universal collapse of DCR versus hold-off time curves can be explained as follows. If we consider primary dark carriers and detrapped carriers within the gate pulse [i.e., first and third terms in (5)], and assume that $P_a N_d$ is so small that all but the first two terms in a Taylor expansion of (4) can be ignored, we obtain the expression for P_d as

$$\boldsymbol{P}_d = \boldsymbol{P}_a \, \boldsymbol{N}_{\mathrm{DM1}} \, \tau \left[1 - \boldsymbol{P}_a \, \frac{c}{1-c} \, \boldsymbol{M}_g \, \frac{\exp\left(\tau/\tau_d\right) - 1}{\exp\left(\boldsymbol{T}_h/\tau_d\right) - 1} \right]^{-1}. \tag{9}$$

In deriving (9), we have made use of the fact that τ is much smaller than the hold-off time T_h so that $\Delta T = \tau + T_h \approx T_h$. The time-independent background DCR is $P_{d,0} = P_a N_{\mathrm{DM1}} \tau$, and the detrapping time can be expressed as
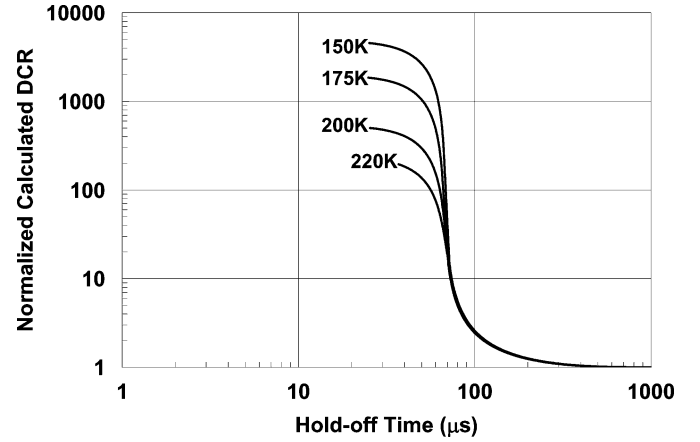

Fig. 4. Collapse of calculated DCR versus hold-off time curves from Fig. 3(a) for device E1.

$\tau_d = \tau_{d,\infty} \exp(E_a/kT)$, where $\tau_{d,\infty}$ is the detrapping time at infinitely high temperature. Given $\tau/\tau_d \ll 1$, we have $[\exp(\tau/\tau_d) - 1] \sim \tau/\tau_d$. Here, c is very small, so $(1-c) \sim 1$. The normalized dark count probability becomes

$$\overline{P_d} = \frac{1}{1 - \tau \, \boldsymbol{M}_g \, \boldsymbol{P}_a \, \frac{c}{\tau_d} \left[\exp\left(\frac{\boldsymbol{T}_h \, e^{-\boldsymbol{E}_a/kT}}{\tau_{d,\infty}}\right) - 1 \right]^{-1}}. \tag{10}$$

Using McIntyre's formalism for calculating avalanche probability P_a [38], we have found $P_a \sim T^{-1/2}$. If $c/\tau_d \sim T^{1/2}$, then the quantity $P_a c/\tau_d$ will be temperature-independent. The rescaling of the hold-off time axis by $\exp(-E_a/kT)$ then yields a single universal functional form for $\overline{\boldsymbol{P}_d}$. This behavior provides useful guidance for subsequent simulations, and in particular, the accuracy of our collapsing procedure for both experimental and simulated results confirms the relationship $c/\tau_d \sim T^{1/2}$.

Applying the modeling formalism described in Section III, we calculate the DCR versus hold-off time behavior illustrated by the solid lines in Fig. 3(a). Although the experimental data exhibit a somewhat more rapid rise in DCR with decreasing hold-off time than the model results, the general agreement is good. The results presented in Fig. 4 confirm that the calculated DCR versus hold-off time curves exhibit the same precise collapse with normalization and rescaling up to differences in the high DCR saturation behavior related to the finite repetition rate of 50 kHz.

For a 40-μm-diameter device from the central region C1, we have performed a similar analysis, with results shown in Fig. 5. To collapse all curves of the measured data to the 150-K curve, the hold-off time axis scaling factor is 1, 1.25, 1.45, and 1.9 for 150, 175, 200, and 220 K data, respectively. From the dependence of these scaling factors on temperature, we find $E_{\mathrm{ap}} \sim 24$ meV.

Comparing results for devices E1 and C1, one finds that the onset of sudden increase in the DCR happens at longer hold-off time for device E1, and the difference between the two devices becomes more significant as the temperature decreases. The activation energy obtained from the rescaling factor is also quite different. From our calculations using $M_g = 10^8$, we find that at
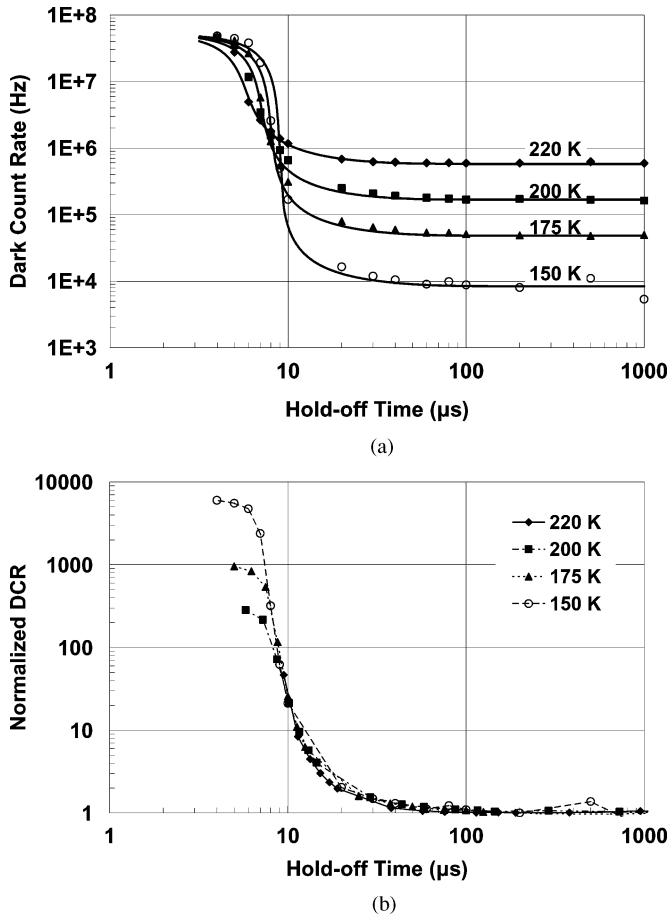
Fig. 5. (a) Experimental (symbols) and simulated (solid lines) DCR versus hold-off time for device C1 at four different temperatures. (b) Collapse of data from (a) after normalization and rescaling.

Fig. 6. Dependence of detrapping time τ_d and trapping ratio c on $1/kT$ for devices E1 and C1, with extracted thermal activation energies.

uncertainties given the much smaller activation energies found for this device.

It is worth noting that in (5) and (7), only one trap level has been considered. While it is straightforward to extend the model to include multiple traps, we do not believe there is a reasonable physical motivation to do so. Moreover, our explanation of the DCR versus hold-off time collapse using (9) and (10) further supports the single trap model, since it is unlikely that a single functional form would adequately describe multiple trap afterpulsing over a wide temperature range. We also point out that attempting to fit a simple exponential curve (or worse yet, multiple exponentials) to the raw data in Figs. 3(a) and 5(a) will not yield meaningful results given the complexity of the afterpulsing process. The physical processes involved include the interaction between afterpulsing events occurring during different gate pulses, and an accurate description of these interactions requires a mathematical form such as (5), as first presented in [19].

B. DCR Versus PDE

As overbias ΔV_{ex} is increased, PDE increases due to the increase of avalanche probability P_a. At the same time, DCR also increases with increasing P_a, as well as with the increase in any field-mediated dark carrier generation. SPAD performance, therefore, always involves a tradeoff between DCR and PDE. To characterize this performance using very short gates, we employ a biasing circuit based on [14]. Gate durations of 1 ns were used, and repetition rate was adjustable, with 500 kHz used as a typical value. The gate pulse amplitude was fixed at 4 V, and the dc offset $V_{br} - V_{dc}$ was set at a value consistent with the target overbias ΔV_{ex}. A pulsed diode laser with wavelength of 1.54 μm and a pulse full-width at half-maximum (FWHM) of 500 ps is attenuated to generate a mean photon number per pulse of 0.1. Gates are generated at a repetition rate R, and optical pulses are turned on during every other gate pulse, yielding an "illuminated gate" repetition rate of $R/2$. As a result of this scheme, there are two different types of gates: one is coincident with the pulsing of the optical source, and the other is interleaved between optical source pulses. The count probabilities of the

150 K the detrapping time of E1 is about six times that of device C1, and the trapped carrier to total carrier ratio c of device E1 is about eight times that of device C1. As temperature increases, the differences of both lifetime and trapping ratio for traps involved in the afterpulsing of the two devices become smaller due to the different value of activation energy. These findings suggest that different traps are involved in the afterpulsing behavior of the edge and center devices.

Fig. 6 shows the dependence on $1/kT$ of detrapping time τ_d and trapping ratio c for devices E1 and C1, respectively. Performing exponential fitting to these curves yields corresponding activation energies. The activation energies obtained for the scaling factor for DCR versus hold-off time collapse (not shown) are identical to those found for τ_d: 91 and 24 meV for devices E1 and C1, respectively. τ_d and c at each temperature can be extracted from fitting it to the experimental data. Activation energies for c are 83.2 and 8.3 meV for devices E1 and C1, respectively. Using $P_a \sim T^{-1/2}$ and deriving an "effective" activation energy for this temperature dependence yields ∼8 meV. For device E1, with $E_a(\tau_d) = 91$ meV and $E_a(c) = 83$ meV, we confirm that $E_a(P_a) + E_a(c) \sim E_a(\tau_d)$, as required for $P_a c/\tau_d$ to be temperature-independent, as discussed earlier. The agreement for device C1 is not as precise, possibly due to larger relative
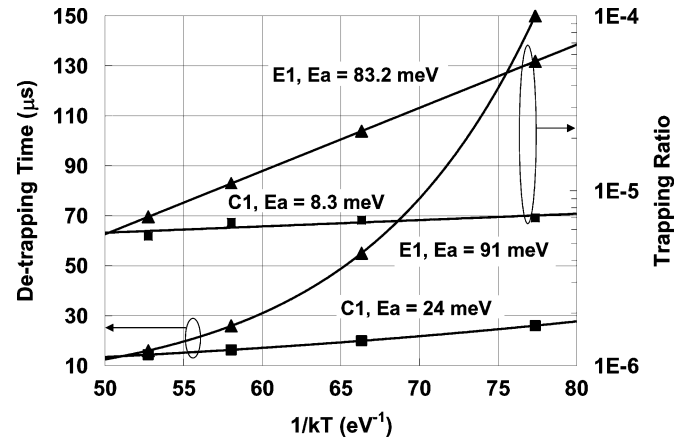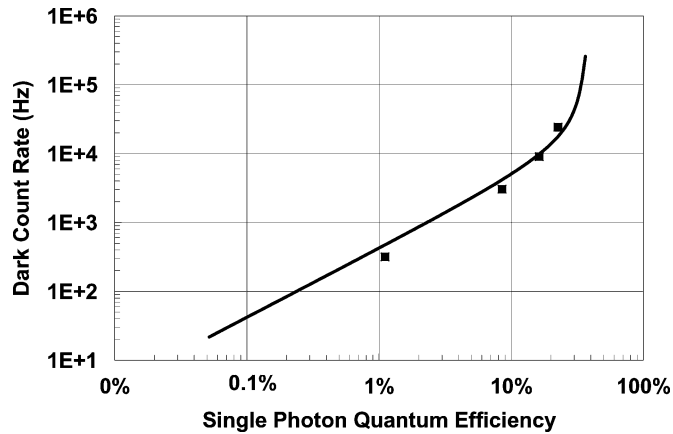
Fig. 7. Experimental (symbols) and simulated (solid lines) DCR versus single photon quantum efficiency for 25-μm-diameter device C2 at 213 K.
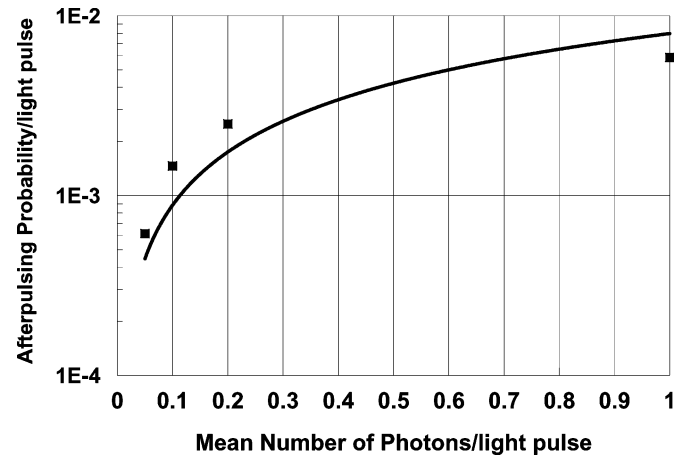

Fig. 8. Experimental (symbols) and simulated (solid lines) AP versus mean photon number for device C2 at 212 K, 500-kHz repetition rate, and overbias corresponding to 22% detection efficiency.

coincident and interleaved pulses are registered separately. In the absence of optical pulses, there is no difference between coincident and interleaved pulses, and the dark count level can be measured at repetition rate R. When optical pulses are present, count probabilities for the coincident and interleaved pulses yield measurements of the PDE and afterpulsing, respectively.

Fig. 7 shows the measured DCR versus SPQE dependence (symbols), as well as calculated results (solid curve), for 213 K. The 25-μm device under study, i.e., C2 is from the center region of the wafer and the afterpulsing behavior of this device can be characterized by a trap similar to that describing the afterpulsing behavior of device C1. At a detection efficiency of 22.5%, the DCR is 2.4×10^4 Hz, corresponding to a dark count probability of 2.4×10^{-5}. Simulated behavior agrees well with the measured data. One notable feature of Fig. 7 is the shape of the DCR versus SPQE curve. If dark carrier generation remains constant with respect to overbias ΔV_{ex} (e.g., when thermal generation dominates), then one would expect DCR and SPQE to increase at the same rate with ΔV_{ex} as dictated by the increase in avalanche probability P_a. The resulting curve on a log–log plot should be linear with a slope of 1, and this behavior is indeed found for SPQE $< 10\%$. For SPQE $> 10\%$, DCR increases faster than SPQE, indicating the onset of nonnegligible tunneling effects, which depend exponentially on the electric field. The influence of afterpulsing on this curve is negligible.

C. Effect of Operating Conditions on Afterpulsing

Afterpulsing limits the repetition rate with which one can arm and operate a SPAD, and is crucial for high count rate applications such as QKD. In addition to intrinsic material properties, afterpulsing depends on various operating conditions, as described in this section.

1) Number of Photons Per Pulse: Afterpulsing depends on the number of carriers flowing through the multiplication region during an avalanche. Since a larger mean photon number per pulse increases the Poisson probability of having multiple primary (i.e., photo-excited) carriers during a single gate, the average number of total carriers per avalanche will increase. Fig. 8 shows the AP per gate versus mean photon number for device
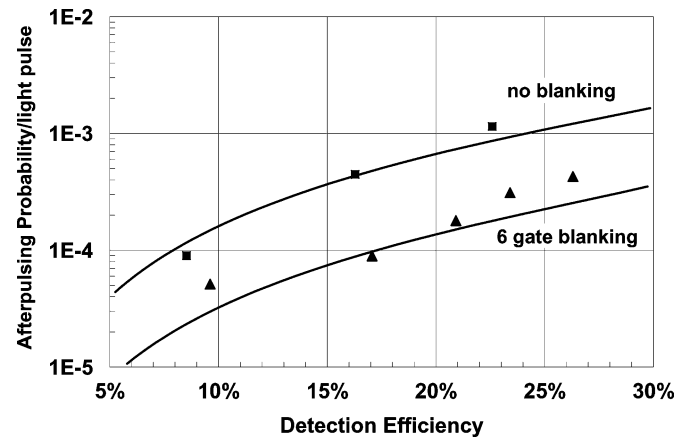

Fig. 9. Experimental (symbols) and simulated (solid lines) AP versus detection efficiency at 213 K, 500-kHz repetition rate, and mean photon number of 0.1, without blanking and with six-gate blanking for device C2.

C2 at 212 K with a 500-kHz repetition rate and an overbias ΔV_{ex} corresponding to a PDE of 22%. Symbols indicate experimental results, and the solid curve was obtained from modeling. The change in mean photon number from 0.05 to 1 results in an increase by a factor of $\sim$10 in AP, with good agreement between experiment and modeling.

2) Blanking: Suppressing gate pulses ("blanking") for some interval following each avalanche event can help to reduce afterpulsing, since it provides more time for the release of trapped carriers, but at the cost of reducing the effective detection efficiency by a dead time factor $[1 + \mu \, \text{DE} \, N_B]^{-1}$, where μ is the mean photon number, DE is the detection efficiency, and N_B is the number of gates blanked after a detection event. Fig. 9 shows the effect of blanking on device C2. At 213 K, with a 500-kHz repetition rate and $\mu = 0.1$, the blanking of six gates results in $\sim$80% reduction in AP, with a dead time correction factor of $\sim$0.89 at a detection efficiency of 20%.

3) Repetition Rate: Fig. 10 shows the calculated dependence of AP on the hold-off time at detection efficiencies of 10% and
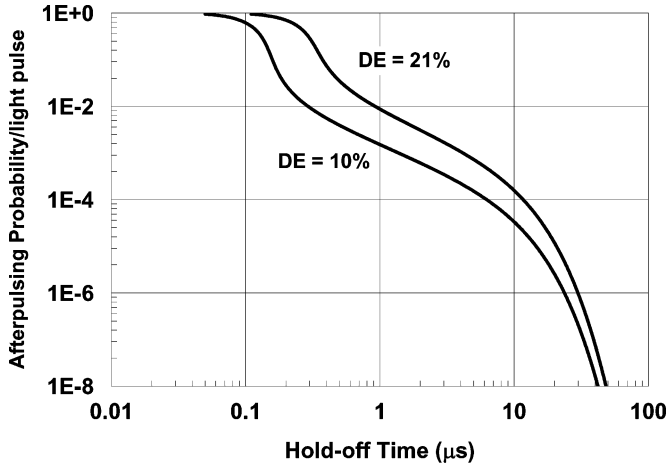
Fig. 10.   Calculated AP versus hold-off time at different detection efficiencies of 10% and 21% and a temperature of 212 K.
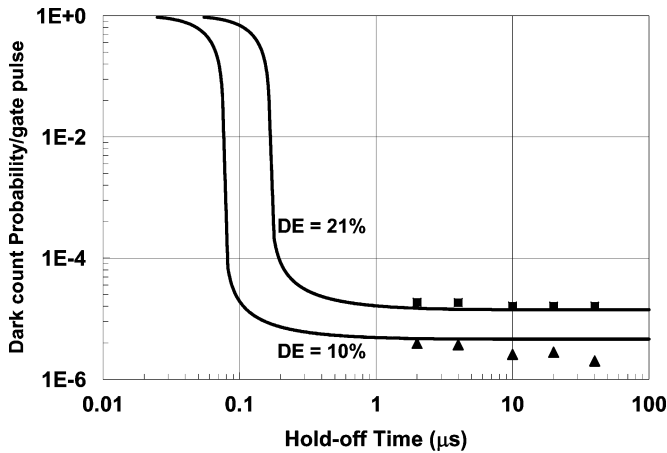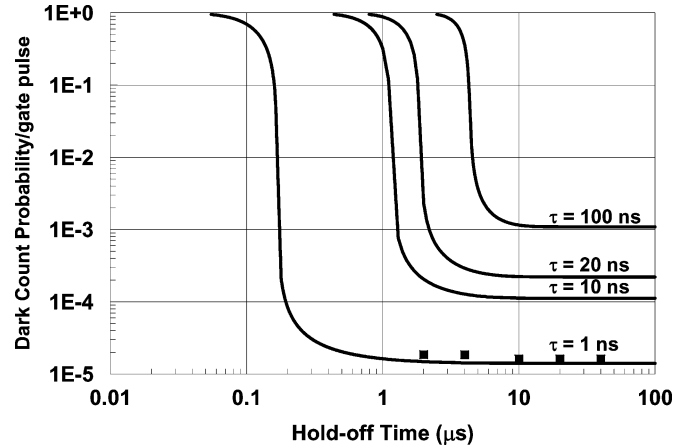

Fig. 12.   Calculated dark count probability versus time between gate pulses for gate durations τ of 1, 10, 20, and 100 ns, at 212 K and 21% detection efficiency (at $\tau = 1$ ns). Corresponding experimental data (from Fig. 11) for $\tau = 1$ ns are also shown.
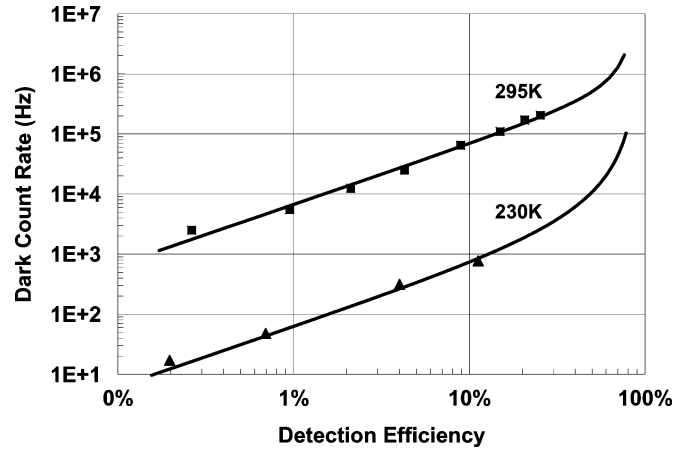

Fig. 11.   Calculated dark count probability versus hold-off time at detection efficiencies of 10% and 21% and a temperature of 212 K. Corresponding experimental data are shown for ≥ 2 μs.

Fig. 13.   Experimental (symbols) and simulated (solid lines) DCR versus detection efficiency for an 80-μm-diameter InGaAsP/InP SPAD at 1.06 μm for 295 and 230 K. Experimental data were obtained for free-running operation.

21%. As already discussed, decreased hold-off time leads to increased afterpulsing. Fig. 11 shows the dependence of dark count probability per gate on hold-off time for detection efficiencies of 10% and 21%. Experimental data was taken for hold-off times between 2 and 40 μs. Calculation shows that the dark count probability increases dramatically for hold-off times less than 0.2 μs (0.1 μs) for 21% (10%) detection efficiency.

4) Pulse Width: Fig. 12 shows the effect of gate width on dark count probability. For longer gates, more primary carriers flow through the multiplication region and increase afterpulsing as described earlier. The results presented here show the benefit of using shorter gates for reducing afterpulsing. In particular, reduction of gate width from 100 to 1 ns reduces the characteristic hold-off time at which afterpulsing sets in strongly by a factor of ~20.

V. DEVICE PERFORMANCE OF 1.06-μm SPADs

The detection of single photons at 1.06 μm is of considerable importance for lidar systems designed for remote sensing and ranging as well as for free-space optical communications in photon-starved applications. The InGaAs/InP SPADs described earlier have good PDE at 1.06 μm, but the use of the narrow bandgap InGaAs absorber results in relatively high DCR. This tradeoff in DCR performance can be much more effectively managed for shorter wavelength detection. To this end, we have developed large area SPADs with InGaAsP quaternary absorbers optimized for operation at 1.06 μm, but otherwise based on the same design platform as the 1.55 μm described earlier. In this section, we present initial results obtained from these devices with free-running operation, and we also show calculated contributions of the dominant mechanisms responsible for DCR in these devices.

Fig. 13 shows the measured DCR versus PDE at a wavelength of 1.06 μm for an 80-μm-diameter device at 295 and 230 K. Free-running photon counting data were obtained using a Poisson source of 1.06-μm photons, the SPAD detector, and a commercial active quenching circuit (AQC) described in [52]. In
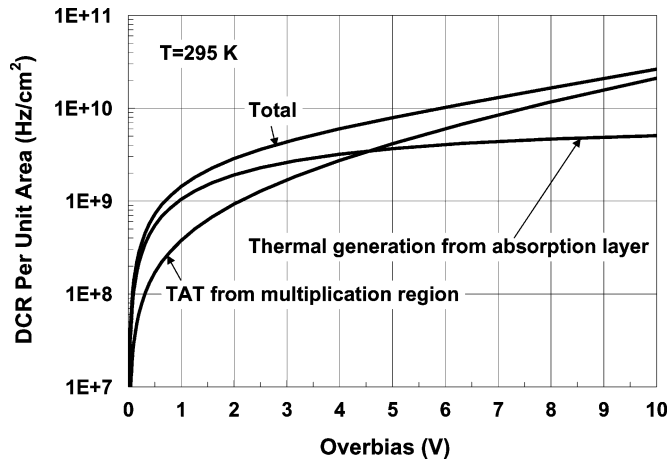
Fig. 14. Calculated dependence of DCR per unit area on overbias for In-GaAsP/InP SPAD at 295 K. Dominant contributions from multiplication region TAT and absorption region thermal generation are also shown.

contrast to the gated mode measurements described for 1.55-μm SPADs, these data were taken by varying the photon flux between 10^0 and 10^8 photons/s and recording the count rate as a function of photon flux. For low photon fluxes ($<10^3$ s^{-1}), we find a constant count rate due to dark counts. For flux values larger than $\sim10^4$ s^{-1}, the count rate increases approximately linearly with photon flux, indicating single photon counting with a dynamic range of three orders of magnitude in photon flux before the count rate saturation. PDE data was obtained from measurements taken at a flux of $\sim10^6$ s^{-1}. Simulated results for both temperatures are also shown, and the calculated correspondence between DCR and PDE agrees with the measured data.

Fig. 14 illustrates the calculated dependence on overbias ΔV_{ex} of DCR per unit area at 295 K. Also shown in the figure are the dominant contributions to DCR, originating from 1) TAT in the multiplication region and 2) thermal generation in the absorption layer; other dark carrier mechanisms (BBT, absorption layer TAT, and multiplication region thermal generation) are insignificant by comparison. The relative importance of multiplication region TAT and absorption region thermal generation depends on the operating temperature and overbias. As in Fig. 14, at 295 K, for overbias voltages less than 4.5 V, absorption layer thermal generation dominates; at higher voltages, multiplication region TAT becomes dominant. In contrast, for the 230-K behavior, multiplication region TAT is at least an order of magnitude larger than absorption region thermal generation for all $\Delta V_{\text{ex}} > 0.2$ V.

VI. Conclusion

In this work, we have performed experimental and computational studies of SPADs designed for 1.55- and 1.06-μm detection. Through the comparison of experimental and modeling results, we can quantitatively describe a number of fundamental performance parameters, including DCR, SPQE, and afterpulsing, over a wide range of operation conditions. We have shown

how DCR depends strongly on hold-off time and operating temperature, with a dramatic increase in DCR at a temperature-dependent characteristic hold-off time dictated by afterpulsing effects. The behavior of DCR versus hold-off time was shown to be described by a universal functional form made apparent by the collapse of data taken over a wide range of temperatures to this universal curve after appropriate DCR normalization and hold-off time rescaling.

Our study of afterpulsing effects has shown that even when a different trap level dominates afterpulsing behavior for devices from different regions of a wafer, a single trap can still accurately account for observed afterpulsing behavior. The relevant characteristic detrapping time and trapping ratio used in our modeling have been extracted, and the dependence of afterpulsing on various operating conditions has been quantified.

Finally, initial results for SPADs optimized for operation at 1.06 μm have been obtained for free-running operation, and detailed modeling for DCR versus PDE shows agreement with the experimental results for these detectors. Additionally, we have shown that multiplication region TAT and absorption region thermal generation dominate other dark carrier generation mechanisms, and that the relative importance of these two dominant mechanisms depends on overbias and temperature. Similar modeling is currently in progress for the 1.55-μm SPADs.

References

[1] B. F. Levine, C. G. Bethea, and J. C. Campbell, "Room temperature 1.3-μm optical time reflectometer using a photon counting InGaAs/InP avalanche detector," *Appl. Phys. Lett.*, vol. 46, no. 4, pp. 333–335, Feb. 1985.

[2] N. Gisin, G. Ribordy, W. Tittel, and H. Zbinden, "Quantum cryptography," *Rev. Mod. Phys.*, vol. 74, no. 1, pp. 145–195, Mar. 2002.

[3] R. G. W. Brown, K. D. Ridley, and J. G. Rarity, "Characterization of silicon avalanche photodiodes for photon-correlation measurements. I: Passive quenching," *Appl. Opt.*, vol. 25, no. 22, pp. 4122–4126, Nov. 1986.

[4] J. G. Rarity and P. R. Tapster, "Experimental violation of Bell's inequality based on phase and momentum," *Phys. Rev. Lett.*, vol. 64, no. 21, pp. 2495–2498, May 1990.

[5] A. L. Lacaita, F. Zappa, S. Bigliardi, and M. Manfredi, "On the bremsstrahlung origin of hot-carrier-induced photons in silicon devices," *IEEE Trans. Electron Devices*, vol. 40, no. 3, pp. 577–582, Mar. 1993.

[6] W. Haecker, O. Groezinger, and M. H. Pilkuhn, "Infrared photon counting by Ge avalanche diodes," *Appl. Phys. Lett.*, vol. 19, no. 4, pp. 113–115, Aug. 1971.

[7] D. S. Bethune and W. P. Risk, "An autocompensating fiber-optic quantum cryptography system based on polarization splitting of light," *IEEE J. Quantum Electron.*, vol. 36, no. 3, pp. 340–347, Mar. 2000.

[8] B. F. Levine and C. G. Bethea, "Single photon detection at 1.3 μm using a gated avalanche photodiode," *Appl. Phys. Lett.*, vol. 44, no. 5, pp. 553–555, Mar. 1984.

[9] A. Lacaita, F. Zappa, S. Cova, and P. Lovati, "Single-photon detection beyond 1 μm: Performance of commercially available InGaAs/InP detectors," *Appl. Opt.*, vol. 35, no. 16, pp. 2986–2996, Jun. 1996.

[10] G. Ribordy, J. Gautier, H. Zbinden, and N. Gisin, "Performance of InGaAs/InP avalanche photodiodes as gated-mode photon counters," *Appl. Opt.*, vol. 37, no. 12, pp. 2272–2277, Apr. 1998.

[11] P. A. Hiskett, G. S. Buller, A. Y. Loudon, J. M. Smith, I. Gontijo, A. C. Walker, P. D. Townsend, and M. J. Robertson, "Performance and design of InGaAs/InP photodiodes for single-photon counting at 1.55 μm," *Appl. Opt.*, vol. 39, no. 36, pp. 6818–6829, Dec. 2000.

[12] D. Stucki, G. Ribordy, A. Stefanov, H. Zbinden, J. G. Rarity, and T. Wall, "Photon counting for quantum key distribution with Peltier cooled InGaAs/InP APDs," *J. Mod. Opt.*, vol. 48, no. 13, pp. 1967–1981, Nov. 2001.

[13] A. Dorokhov, A. Glauser, Y. Musienko, C. Regenfus, S. Reucroft, and J. Swain, "Recent progress on cooled avalanche photodiodes for single photon detection," *J. Mod. Opt.*, vol. 51, no. 9–10, pp. 1351–1357, Jun. 2004.

[14] D. S. Bethune, W. P. Risk, and G. W. Pabst, "A high-performance integrated single-photon detector for telecom wavelengths," *J. Mod. Opt.*, vol. 51, no. 9–10, pp. 1359–1368, Jun. 2004.

[15] A. Trifonov, D. Subacius, A. Berzanskis, and A. Zavriyev, "Single photon counting at telecom wavelength and quantum key distribution," *J. Mod. Opt.*, vol. 51, no. 9–10, pp. 1399–1415, Jun. 2004.

[16] M. A. Itzler, R. Ben-Michael, C. F. Hsu, K. Slomkowski, A. Tosi, S. Cova, F. Zappa, and R. Ispasoiu, "Single photon avalanche diodes (SPADs) for 1.5 μm photon counting applications," *J. Mod. Opt.*, vol. 54, no. 2–3, pp. 283–304, Feb. 2007.

[17] R. Ben-Michael, M. A. Itzler, B. Nyman, and M. Entwistle, "Afterpulsing in InGaAs/InP single photon avalanche photodetectors," in *Proc. 2006 Dig. LEOS Summer Top. Meet.*, pp. 15–16.

[18] S. Pellegrini, R. E. Warburton, L. J. J. Tan, J. S. Ng, A. B. Krysa, K. Groom, J. P. R. David, S. Cova, M. J. Robertson, and G. S. Buller, "Design and performance of an InGaAs-InP single-photon avalanche diode detector," *IEEE J. Quantum Electron.*, vol. 42, no. 4, pp. 397–403, Apr. 2006.

[19] Y. Kang, H. X. Lu, Y.-H. Lo, D. S. Bethune, and W. P. Risk, "Dark count probability and quantum efficiency of avalanche photodiodes for single-photon detection," *Appl. Phys. Lett.*, vol. 83, no. 14, pp. 2955–2957, Oct. 2003.

[20] D. A. Ramirez, M. M. Hayat, G. Karve, J. C. Campbell, S. N. Torres, B. E. A. Saleh, and M. C. Teich, "Detection efficiencies and generalized breakdown probabilities for nanosecnd-gated near infrared single-photon avalanche photodiodes," *IEEE J. Quantum Electron.*, vol. 42, no. 2, pp. 137–145, Feb. 2006.

[21] K. Sugihara, E. Yagyu, and Y. Tokuda, "Numerical analysis of single photon detection avalanche photodiodes operated in the Geiger mode," *J. Appl. Phys.*, vol. 99, no. 12, pp. 124502–1–124502-5, Jun. 2006.

[22] A. Spinelli and A. L. Lacaita, "Physics and numerical simulation of single photon avalanche diodes," *IEEE Trans. Electron. Devices*, vol. 44, no. 11, pp. 1931–1943, Nov. 1997.

[23] K. A. McIntosh, J. P. Donnelly, D. C. Oakley, A. Napoleone, S. D. Calawa, L. J. Mahoney, K. M. Molvar, E. K. Duerr, S. H. Groves, and D. C. Shaver, "InGaAsP/InP avalanche photodiodes for photon counting at 1.06 μm," *Appl. Phys. Lett.*, vol. 81, no. 14, pp. 2505–2507, Sep. 2002.

[24] K. E. Jensen, P. I. Hopman, E. K. Duerr, E. A. Dauler, J. P. Donnelly, S. H. Groves, L. J. Mahoney, K. A. McIntosh, K. M. Molvar, A. Napoleone, D. C. Oakley, S. Verghese, C. J. Vineis, and R. D. Younger, "Afterpulsing in Geiger-mode avalanche photodiodes for 1.06 μm wavelength," *Appl. Phys. Lett.*, vol. 88, no. 13, pp. 133503–1–133503-3, Mar. 2006.

[25] J. P. Donnelly, E. K. Duerr, K. A. McIntosh, E. A. Dauler, D. C. Oakley, S. H. Groves, C. J. Vineis, L. J. Mahoney, K. M. Molvar, P. I. Hopman, K. E. Jensen, G. M. Smith, S. Verghese, and D. C. Shaver, "Design considerations for 1.06-μm InGaAsP-InP Geiger-mode avalanche photodiodes," *IEEE J. Quantum Electron.*, vol. 42, no. 8, pp. 797–809, Aug. 2006.

[26] E. A. Dauler, P. I. Hopman, K. A. McIntosh, J. P. Donnelly, E. K. Duerr, R. J. Magliocco, L. J. Mahoney, K. M. Molvar, A. Napoleone, D. C. Oakley, and F. J. O'Donnell, "Scaling of dark count rate with active area in 1.06 μm photon-counting InGaAsP/InP avalanche photodiodes," *Appl. Phys. Lett.*, vol. 89, no. 11, pp. 111102–1–11102-3, Sep. 2006.

[27] M. A. Itzler, X. D. Jiang, R. Ben-Michael, K. Slomkowski, M. A. Krainak, S. Wu, and X. L. Sun, "InGaAsP/InP avalanche photodetectors for non-gated 1.06 μm photon-counting receivers," *Proc. SPIE*, vol. 6572, pp. 65720G–1–65720G-10, May 2007.

[28] K. Nishida, K. Taguchi, and Y. Matsumoto, "InGaAsP heterostructure avalanche photodiodes with high avalanche gain," *Appl. Phys. Lett.*, vol. 35, no. 3, pp. 251–253, Aug. 1979.

[29] S. R. Forrest, O. K. Kim, and R. G. Smith, "Optical response time of $In_{0.53}Ga_{0.47}$ As/InP avalanche photodiodes," *Appl. Phys. Lett.*, vol. 41, no. 1, pp. 95–98, Jul. 1982.

[30] Y. Liu, S. R. Forrest, J. Hladky, M. J. Lange, G. H. Olsen, and D. E. Ackley, "A planar InP/InGaAs avalanche photodiode with floating guard ring and double diffused junction," *J. Lightw. Technol.*, vol. 10, no. 2, pp. 182–193, Feb. 1992.

[31] M. A. Itzler, C. S. Wang, S. McCoy, N. Codd, and N. Komaba, "Planar bulk-InP avalanche photodiode design for 2.5 and 10 Gb/s applications," in *Proc. 24th Eur. Conf. Opt. Commun.*, 1998, vol. 1, pp. 59–60.

[32] M. A. Itzler, K. K. Loi, S. McCoy, N. Codd, and N. Komaba, "Manufacturable planar bulk-InP avalanche photodiodes for 10 Gb/s applications," in *Proc. 12th Annu. Meet. Lasers Electro-Opt. Soc.*, 1999, vol. 2, pp. 748–749.

[33] M. A. Itzler, K. K. Loi, S. McCoy, N. Codd, and N. Komaba, "High-performance, manufacturable avalanche photodiodes for 10 Gb/s optical receivers," in *Proc. 25th Opt. Fiber Commun. Conf.*, 2000, vol. 4, pp. 126–128.

[34] S. M. Sze, *Physics of Semiconductor Devices*. New York: Wiley, 1981, pp. 520–527.

[35] B. E. A. Saleh, M. M. Hayat, and M. C. Teich, "Effect of dead space on the excess noise factor and time response of avalanche photodiodes," *IEEE Trans. Electron Devices*, vol. 37, no. 9, pp. 1976–1984, Sep. 1990.

[36] R. J. McIntyre, "A new look at impact ionization-part I: A theory of gain, noise, breakdown probability, and frequency response," *IEEE Trans. Electron Devices*, vol. 46, no. 8, pp. 1623–1631, Aug. 1999.

[37] F. Zappa, P. Lovati, and A. Lacaita, "Temperature dependence of electron and hole ionization coefficients in InP," in *Proc. Int. Conf. Indium Phosphide Related Mater.*, 1996, pp. 628–631.

[38] R. J. McIntyre, "On the avalanche initiation probability of avalanche diodes above the breakdown voltage," *IEEE Trans. Electron Devices*, vol. ED-20, no. 7, pp. 637–641, Jul. 1973.

[39] S. Adachi, "Optical dispersion relations for GaP, GaAs, GaSb, InP, InAs, InSb, Al_xGa_{1-x}As and $In_{1-x}Ga_xAs_yP_{1-y}$," *J. Appl. Phys.*, vol. 66, no. 12, pp. 6030–6040, Dec. 1989.

[40] R. H. Kingston, "Electroabsorption in GaInAsP," *Appl. Phys. Lett.*, vol. 34, no. 11, pp. 744–746, Jun. 1979.

[41] I. Vurgaftman, J. R. Meyer, and L. R. Ram-Mohan, "Band parameters for III-V compound semiconductors and their alloys," *J. Appl. Phys.*, vol. 89, no. 11, pp. 5815–5875, Jun. 2001.

[42] S. R. Forrest and O. K. Kim, "Deep levels in $In_{0.53}Ga_{0.47}$As/InP heterostructures," *J. Appl. Phys.*, vol. 53, no. 8, pp. 5738–5745, Aug. 1982.

[43] F. Buchali, R. Behrendt, and G. Heymann, "InGaAsP/InP-photodiodes with dark current limited by generation-recombination," *Electron. Lett.*, vol. 27, no. 3, pp. 235–237, Jan. 1991.

[44] J. M. Martin, S. Garcia, I. Martil, G. Gonzalez-Diaz, E. Castan, and S. Duenas, "Deep-level transient spectroscopy and electrical characterization of ion-implanted p-n junctions into undoped InP," *J. Appl. Phys*, vol. 78, no. 9, pp. 5325–5330, Nov. 1995.

[45] T. Sugino, H. Ninomiya, T. Yamada, J. Shirafuji, and K. Matsuda, "Creation and passivation of electron traps in n-InP treated with hydrogen plasma," *Appl. Phys. Lett.*, vol. 60, no. 10, pp. 1226–1228, Mar. 1992.

[46] S. H. Chiao and G. A. Antypas, "Photocapacitance effects of deep traps in n-type InP," *J. Appl. Phys.*, vol. 49, no. 1, pp. 466–468, Jan. 1978.

[47] O. Wada, A. Majerfeld, and A. N. M. M. Choudhury, "Interaction of deep-level traps with the lowest and upper conduction minima in InP," *J. Appl. Phys.*, vol. 51, no. 1, pp. 423–432, Jan. 1980.

[48] G. J. Shaw, S. R. Messenger, R. J. Walters, and G. P. Summers, "Radiation-induced reverse dark currents in $In_{0.53}Ga_{0.47}$As photodiodes," *J. Appl. Phys.*, vol. 73, no. 11, pp. 7244–7249, Jun. 1993.

[49] P. Philippe, P. Poulain, K. Kazmierski, and B. de Cremoux, "Dark-current and capacitance analysis of InGaAs/InP photodiodes grown by metalorganic chemical vapor deposition," *J. Appl. Phys.*, vol. 59, no. 5, pp. 1771–1773, Mar. 1986.

[50] K. Kazmierski, P. Philippe, P. Poulain, and B. de Cremoux, "C-V measurement and modelization of GaInAs/InP heterointerface with traps," *J. Appl. Phys.*, vol. 61, no. 5, pp. 1941–1946, Mar. 1987.

[51] Y. Takanashi and N. Kondo, "Deep trap in InGaAs grown by gas source molecular beam epitaxy," *J. Appl. Phys.*, vol. 85, no. 1, pp. 633–634, Jan. 1999.

[52] S. Cova, M. Ghioni, A. Lacaita, C. Samori, and F. Zappa, "Avalanche photodiodes and quenching circuits for single-photon detection," *Appl. Opt.*, vol. 35, no. 12, pp. 1956–1976, Apr. 1996.

Xudong Jiang received the B.S., M.S., and Ph.D. degrees in physics from Peking University, Beijing, China, in 1989, 1992 and 1995, respectively.

He was a Postdoctoral Researcher at Harvard University, Cambridge, MA (1995–1996) and Princeton University, Princeton, NJ (1996–1997), working on electrical and optical properties of superlattices and thin film transistors. He joined the University of Florida, Gainesville, FL, as co-principal investigator on a project funded by the US Army Research Office and focused on MWIR and LWIR quantum well infrared photodetectors (QWIPs) design, processing, and characterization during 1997–2000. He joined Multiplex, Inc., South Plainfield, NJ, in 2000 as a Member of Technical Staff and became a Distinguished Member of Technical Staff in 2002 and a Manager of laser engineering and operation in 2003, working on the development and manufacturing of 980 nm pump laser and electroabsorption modulated laser (EML) chips and modules. In 2006, he joined Princeton Lightwave Inc., Cranbury, NJ, as a Senior Staff Engineer, working on the design, analysis, and characterization of photodetectors.

Mark A. Itzler (M'96–SM'07) received the B.S. degree in physics from Brown University, Providence, RI, and the Ph.D. degree in physics from the University of Pennsylvania, Philadelphia, PA, in 1986 and 1992, respectively.

From 1992 to 1995, he was a Postdoctoral Researcher at Harvard University, Cambridge, MA, working on low-temperature superconductors. In 1996, he joined Epitaxx Optoelectronics, Inc., West Trenton, NJ, where he began research and development on near-infrared photodetectors, and became the Director of its R&D in 1999. Then, he became a Chief Technical Officer and Vice President of device engineering at JDS Uniphase, which acquired Epitaxx. In 2003, he became a Chief Technical Officer at Princeton Lightwave Inc., Cranbury, NJ. He has authored about 35 technical papers and conference proceeding presentations.

Dr. Itzler is a member of the IEEE LEOS Technical Committee on Photodetectors and Imaging, where he was the Technical Committee Chair from 2002 to 2004.

Rafael Ben-Michael received the B.A., M.S., and Ph.D. degrees in physics and electrooptics, in 1987, 1989, and 1993, respectively, all from the Technion – Israel Institute of Technology, Haifa, Israel.

In 1993, he joined Bell Laboratories, Murray Hill, NJ, as a Postdoctoral Researcher, working on InP-based lasers and photonic-integrated circuits. In 2001, he joined the Epitaxx division of JDS Uniphase as a Device Design Manager, responsible for the development of 40-GHz PIN photodetector and the continuous improvement of APDs to improve APD performance and tailor APD design parameters to different applications. In 2004, he joined Princeton Lightwave, Inc., Cranbury, NJ, as a Principal Scientist developing high performance photodetector and laser technology.

Krystyna Slomkowski received the B.A. degree in microbiology from Douglass College, Rutgers University, New Brunswick, NJ, in 1976.

In 1978, she joined the Laser Diode Laboratories, Edison, NJ, as a Senior Process Technician, responsible for all processing of GaAs Burrus LEDs. In 1985, she joined Epitaxx Optoelectronics, Inc., West Trenton, NJ, as a Senior Process Engineer, where she was responsible for the process development of planar InGaAs-InP p-i-n photodiodes and establishing a manufacturing line for this product. In 1989, she joined the R&D Development Group and in 1999 she became the Technical Manager of the Process Development Group at the Epitaxx Division of JDS Uniphase. In January 2004, she joined Princeton Lightwave, Inc., Cranbury, NJ, as a Senior Staff Engineer, where she is responsible for photodetector and laser diode process development and execution.